

Research Article

A Preliminary Research on Combustion Characteristics of a Novel-Type Scramjet Combustor

Linqing Zhang,¹ Juntao Chang,¹ Wenxiang Cai ,² Hui Sun,³ and Yingkun Li ²

¹School of Energy Science and Engineering, Harbin Institute of Technology, Harbin 150000, China

²School of Mechanical Engineering, Nanjing University of Science and Technology, Nanjing 210094, China

³AECC Commercial Aircraft Engine Co., Ltd., Shanghai 201306, China

Correspondence should be addressed to Wenxiang Cai; caiwx_2005@njjust.edu.cn

Received 13 July 2022; Revised 21 November 2022; Accepted 6 December 2022; Published 30 December 2022

Academic Editor: Zhen-Yu Tian

Copyright © 2022 Linqing Zhang et al. This is an open access article distributed under the Creative Commons Attribution License, which permits unrestricted use, distribution, and reproduction in any medium, provided the original work is properly cited.

In this work, a new configuration of strut-based scramjet is proposed, and a series of simulations are conducted to investigate its possibility of practical application. The simulation results are verified via the classical DLR ramjet and an experiment conducted on the connected pipe facility. The inlet area (A_{in}) and air intake height (H) of the combustor are varied independently to investigate their performance. The results indicate that the flow field and shock wave structure of such engine reveal similar characteristics as the classical DLR engine, and the variation in engine geometry can significantly affect its combustion characteristics. Moreover, the combustion efficiency could be enhanced by 2% as the A_{in} varied from $900\pi \text{ mm}^2$ to $1100\pi \text{ mm}^2$; increasing the air intake path (H) to 12 mm can increase the combustion efficiency by 25%. In general, the present work proposes a new geometry of the scramjet combustor; this combustor has possibility of practical application, but a further and detailed investigation is still needed.

1. Introduction

The supersonic combustion ramjet draws attention throughout the world owing to its characteristics of simple structure, high speed, and low cost [1]. There are many researchers who have conducted a lot of efforts on the combustion characteristics of scramjet combustors; they found that the structure of the combustor plays a critical role in flame stabilization and its performance [2–5].

So far, there are three types of the typical structures of scramjet combustor, i.e., the cavity- [2, 3, 6–15], strut- [5, 16], and backward-facing step-based combustor [4, 17–20]. The strut-based combustor was first proposed by Waidmann et al. [21]; they used hydrogen as the fuel to investigate the combustion characteristic of a typical strut-based scramjet combustor (DLR (German Aerospace Center) scramjet) via experimental approach; in this investigation, the flow features were clearly captured, and the chamber pressure was found to be enhanced with increasing of hydrogen mass flow rate. At the same time, the 2D cavity-based scramjet combustor fueled by kerosene and hydrogen was investigated by

Vinogradov et al. [22]; the results indicated that the performance of the scramjet was highly dominated by the ignition and combustion process. After that, the backward-facing step-based scramjet was proposed by Witt [23] and Angus [24] from the Naval Postgraduate School; they used PMMA as fuel, and the engine was ignited using a pilot torch fueled by hydrogen; the research confirmed the feasibility of backward-facing step-based combustor in scramjet.

With the deepening of researchers' understanding of supersonic combustion, they noticed that enhancing combustion and mixing efficiency is the most effective method to improve the engine performance [25]. Thus, with the enrichment and development of various research methods, many researchers have conducted a lot of efforts to enhance the mixing and combustion efficiency by modifying the structure of the scramjet combustor, including changing the strut or cavity configuration [26], using multiple cavities [27–31] and so on. Sun et al. [31] conducted an investigation of the ignition process of hydrogen-fueled scramjet combustor; in such combustor, multicavities were involved. The results indicated that the multiple cavities were helpful to the diffusion of the fuel, and the

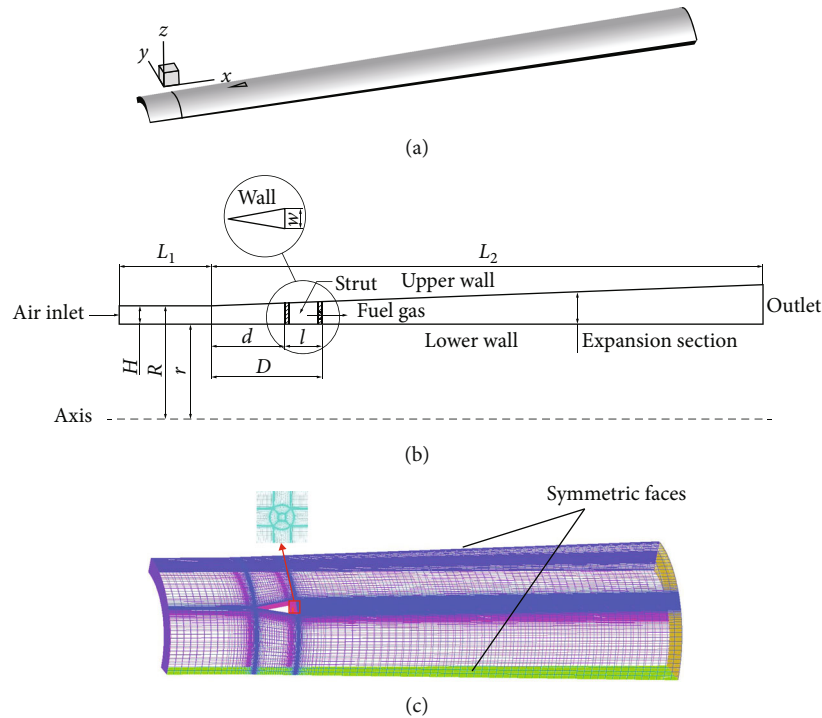


FIGURE 1: Physical model of the SFRJ used in this investigation.

location of the fuel injector played an important role in the fuel ignition performance. Huang [16] conducted an investigation on the effect of strut configurations of a typical strut-based DLR-type combustor. The effect of different radii of the strut tips on the combustion characteristics is studied, which varied from 0.211 mm to 2.853 mm. The results indicated that the shock wave system around the strut became more complicated as the radius was increased. And the combustion efficiency was highly related to the shock wave structure led by the strut configuration. Kummitha et al. [11, 32–34], Pandey et al., and Choubey et al. [35–38] conducted numerous investigations that attempted to obtain a higher combustion efficiency; they used different strut types of injectors and combustion chambers. The research reported that the combustion and mixing efficiency could be highly dominated by the engine geometry.

With the development of experimental and analytical technology, recently, many researchers have made many detailed explorations of the effect of the structure of the scramjet combustor on its performance. Yang et al. [30] conducted an investigation of the multicavity solid-fueled scramjet; the influence of cavity shape on the characteristics of such combustors was studied. They investigated three types of cavities, i.e., flame-holding, narrow, and lobe cavities; the results indicated that the mixing and combustion efficiency could be significantly improved under the structure of narrow and lobe cavities. Meanwhile, Yang et al. [39] studied the injection structure of the same type of scramjet. In this research, the injector had three types of structure, i.e., circular at 60° , elliptical at 90° , and two-stage elliptical at 60° ; they reported that the elliptical at 90° -type injector had the ability to improve the ignition and combustion performance, and the two-stage elliptical at 60° -type injector could enhance the combustion frequency compared to that of the cir-

cular at 60° -type injector. Recently, Kireeti et al. [40] numerically investigated the combustion characteristics of four strut injectors and doubly-dual cavity-based scramjet combustor. In this research, the four struts were cross-symmetrically distributed ahead of the doubly-dual cavity. The results indicated that a better mixing of the fuel and inlet air was obtained in such cases owing to the increased level of the shock layer. In addition to the influence of the flame holder structures, the structure of the engine isolator may also affect the engine performance. Motivated by this, Sharma et al. [41] conducted a numerical investigation on the influence of isolator section on the scramjet performance. The isolator length varied from $2.5D$ to $55D$, where D represented the diameter of the injector. The results revealed that the variation of the isolator length could marginally enhance the mixing rate, and they found that the Prandtl-Meyer expansion fan generated at the flame holder could effectively isolate the combustor and isolator; thus, they concluded that the isolator could be designed based on the flow homogenization of the inlet air ahead of the combustor.

The aforementioned combustor mainly focused on the two-dimensional shape (square cavity), which may increase the difficulty in practical applications of the scramjet and on the other hand increase the space occupancy of the engine. By this, the present research proposes a novel strut-based configuration of the engine, which is the annular strut-based combustor, and the combustion characteristics in different combustor geometry are discussed.

In the present paper, the novel strut-based configuration of the scramjet was proposed, and preliminary research has been conducted. The governing equations and the models are introduced, and the simulation cases are validated against the benchmark cases, which are illustrated in Section 2. The model is then

applied to evaluate the combustion and mixing characteristics of such combustor under the effect of (1) air intake height (H) and (2) air intake area (A_{in}); this is described and discussed in Section 3. The key findings are summarized in Section 4.

2. Mathematical Method

2.1. Governing Equations of Fluid Domain. The governing equations of fluid domain could be written in the form

below:

$$\frac{\partial Q}{\partial t} + \frac{\partial E}{\partial x} + \frac{\partial F}{\partial y} + \frac{\partial H}{\partial z} = \frac{\partial E_v}{\partial x} + \frac{\partial F_v}{\partial y} + \frac{\partial H_v}{\partial z} + S, \quad (1)$$

where $Q, E, F, E_v, F_v, H, H_v,$ and S are expressed in the following form:

$$\begin{aligned} Q &= \begin{bmatrix} \rho \\ \rho u \\ \rho v \\ \rho w \\ \rho E \\ \rho c_i \end{bmatrix}, \\ E &= \begin{bmatrix} \rho u \\ \rho u^2 + p \\ \rho uv \\ \rho uw \\ (\rho E + p)u \\ \rho u c_i \end{bmatrix}, \\ F &= \begin{bmatrix} \rho v \\ \rho v^2 + p \\ \rho uv \\ \rho vw \\ (\rho E + p)v \\ \rho v c_i \end{bmatrix}, \\ H &= \begin{bmatrix} \rho w \\ \rho w^2 + p \\ \rho vw \\ (\rho E + p)w \\ \rho w c_i \end{bmatrix}, \\ E_v &= \begin{bmatrix} 0 \\ \tau_{xx} \\ \tau_{xy} \\ \tau_{xz} \\ u\tau_{xx} + v\tau_{xy} + w\tau_{xz} + q_x + \sum_{i=1}^N \rho D_{m,i} h_i \frac{\partial c_i}{\partial x} \\ \rho D_m \frac{\partial c_i}{\partial x} \end{bmatrix}, \\ F_v &= \begin{bmatrix} 0 \\ \tau_{xy} \\ \tau_{yy} \\ \tau_{yz} \\ u\tau_{xy} + v\tau_{yy} + w\tau_{yz} + q_y + \sum_{i=1}^N \rho D_{m,i} h_i \frac{\partial c_i}{\partial y} \\ \rho D_m \frac{\partial c_i}{\partial y} \end{bmatrix}, \\ H_v &= \begin{bmatrix} 0 \\ \tau_{xz} \\ \tau_{yz} \\ \tau_{zz} \\ u\tau_{xz} + v\tau_{yz} + w\tau_{zz} + q_z + \sum_{i=1}^N \rho D_{m,i} h_i \frac{\partial c_i}{\partial z} \\ \rho D_m \frac{\partial c_i}{\partial z} \end{bmatrix}, \\ S &= \begin{bmatrix} S_p \\ S_{\rho u} \\ S_{\rho v} \\ S_{\rho w} \\ S_{\rho E} \\ m_i + S_{\rho i} \end{bmatrix}. \end{aligned} \quad (2)$$

The τ is shear stress, and $q_x, q_y,$ and q_z represent the heat fluxes in $x, y,$ and z directions. Considering the multicomponent involved in the combustion field, ρD_i is utilized to represent the diffusion of each component and could be calculated by

$$\rho D_i = \frac{1 - X_i}{1 - c_i} \left(\frac{\mu_l}{S_c} + \frac{\mu_t}{S_{ct}} \right). \quad (3)$$

Meanwhile, to calculate the viscosities of the gas mixture accurately, the Lennard-Jones equation is applied (as shown in Equation (4)). And the laminar and turbulent viscosities ($\mu_{li/j}$ and $\mu_{ti/j}$) of the mixture are calculated using the

following formula:

$$\begin{aligned} \mu_l &= \sum_{i=1}^7 \frac{X_i \mu_{li}}{\phi_i}, \quad \phi_i = \sum_{j=1}^7 \frac{X_j \left[1 + \sqrt{\mu_{li}/\mu_{lj}} (M_i/M_j)^{1/4} \right]^2}{\sqrt{8(1 + (M_i/M_j))}}, \\ \mu_t &= \frac{a_1 \rho k}{\max(a_1 \omega, f_2 \Omega)}, \quad f_2 = \tanh \left[\max \left(2 \frac{\sqrt{k}}{0.99 \omega y^l}, \frac{500 \mu}{\rho y^2 \omega} \right) \right]^2. \end{aligned} \quad (4)$$

The equation shown below is employed to calculate the

TABLE 1: (a) Geometry parameters of the present model; (b) detailed boundary condition.

(a)								
L_1	L_2	H	R	r	d	D	w	D_t
50 mm	300 mm	10 mm	55 mm	45 mm	10 mm	38 mm	10 mm	4 mm
(b)								
Inlet	Pressure (MPa)			Temperature (K)			Velocity (m/s)	
	1.5			650			762	
Fuel nozzle	Pressure (MPa)			Temperature (K)			Velocity (m/s)	
	2			1800			1362	
Outlet	Pressure (Pa)			Temperature (K)				
	101325			300				
Symmetric faces	Symmetric boundary condition							
Walls	Nonslip adiabatic boundary condition							

TABLE 2: Simulation conditions.

Case number	R/mm	r/mm	H/mm	A_{in}/mm^2
Case 1	60	50	10	1100π
Case 2	55	45	10	1000π
Case 3	50	40	10	900π
Case 4	66.5	58.5	8	1000π
Case 5	47.65	35.65	12	1000π

thermal conductivity λ .

$$\lambda = \frac{\mu_l c_p}{Pr_l} + \frac{\mu_t c_p}{Pr_t}. \quad (5)$$

The pressure of gas mixture is given by Equation (6), and the Newton iteration method is used to calculate the temperature (T) of the flow field.

$$p = \sum_{i=1}^7 \frac{\rho_i}{M_i} R_u T, \quad (6)$$

$$\rho E - \frac{1}{2} \rho (u^2 + v^2 + w^2) = \sum_{i=1}^7 \rho_i \left(\int_{298}^T C_{pi} dT + h_i^{298} \right) - R_u T \sum_{i=1}^7 \frac{\rho_i}{M_i}, \quad (7)$$

where the C_{pi} used in Equation (7) is defined by Equation (8); the parameter α_{ki} ($k = 1, 2, 3, 4, 5$) can be found in the chemical kinetics package:

$$C_{pi} = a_{1i} + a_{2i}T + a_{3i}T^2 + a_{4i}T^3 + a_{5i}T^4. \quad (8)$$

2.2. Numerical Solution Method. In this research, the ANSYS Fluent 2019 is utilized to simulate the flow features in the present model. And to capture the shock wave lead by the

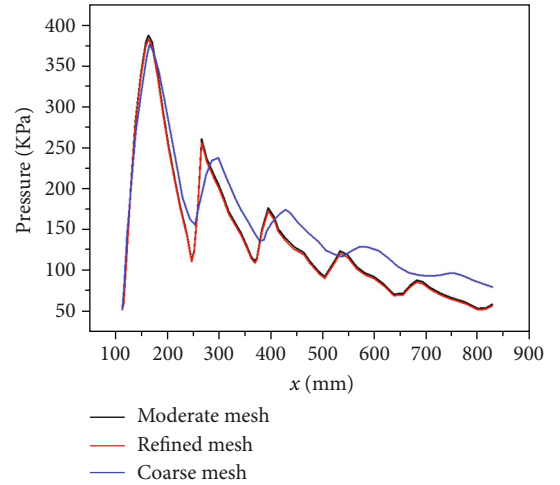


FIGURE 2: Results of grid independency study.

supersonic flow in such systems more accurately, the monotone upstream-centered scheme for conservation laws (MUSCL) and advection upstream-splitting method by pressure-based weight function (AUSM) scheme are utilized to compute convective flux quantities. And, owing to the existence of the shear flow and flow separation phenomenon in the present scramjet combustor, the $k-\omega$ SST (shear-stress transport) turbulence model proposed by Menter is used to simulate the turbulent flow in this research.

2.3. Chemical Reaction Model. The chemical reaction kinetic of CO and H_2 mixture in the scramjet is described as Equations (9) and (10); we use a simplified one-step mechanism to simulate the reaction between the CO, H_2 , and O_2 . In this research, for the consideration of the effect of turbulence and high-speed flow in the scramjet, the finite rate/eddy dissipation model is applied to simulate the chemical reaction processes. The combustion mechanism is shown below. And the

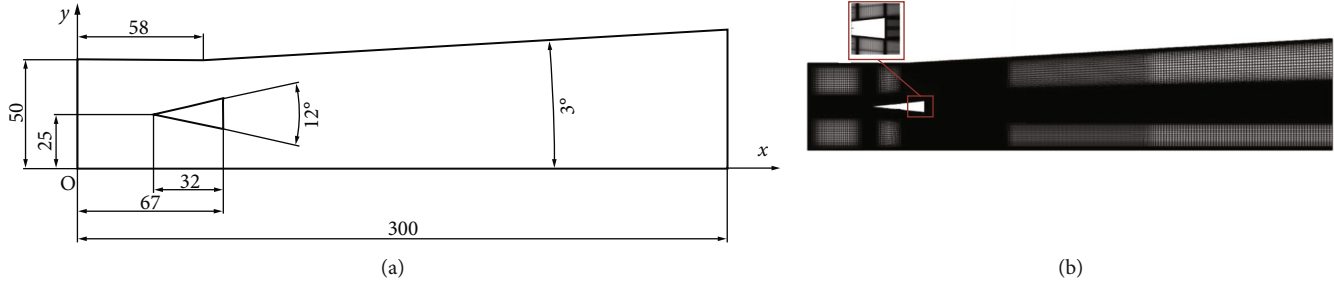
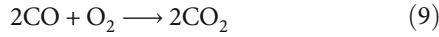


FIGURE 3: Physical model of DLR engine.

TABLE 3: Boundary conditions.

	Air inlet	H ₂ inlet
Inlet Mach number	2.0	1.0
Velocity (m/s)	730	1200
Temperature (K)	340	250
Pressure (Pa)	100000	100000
Mass fraction of N ₂	0.736	0
Mass fraction of O ₂	0.232	0
Mass fraction of H ₂ O	0.032	0
Mass fraction of H ₂	0	1

other parameters such as preexponential factors, activation energy, and temperature exponent could be obtained from the CHEMKIN kinetic package.



2.4. Physical Model and Boundary Conditions. The physical model of the present research is an annular combustion chamber model, which is shown in Figure 1. And, to reduce the computational cost, 1/4 of the model is selected, as shown in Figure 1(a). In Figure 1(b), the value of L_1 , L_2 , H , R , r , d , D , and w is 50 mm, 300 mm, 10 mm, 55 mm, 45 mm, 10 mm, 38 mm, and 10 mm, respectively (see Table 1(a)). There are four struts placed along the circumferential direction, and a fuel nozzle with a diameter of $D_t = 4$ mm is set at the middle of each strut bottom. The boundary conditions can be summarized as follows (see Figures 1(b) and 1(c)): (1) the inlet condition is set with the constant total pressure, temperature, and velocity of 1.5 MPa, 650 K, and 762 m/s, respectively; (2) pressure outlet condition at the engine outlet is set with the pressure of 101325 Pa and 300 K in temperature; (3) the symmetric boundary condition is utilized at two symmetric faces; (4) nonslip adiabatic boundary condition is employed at walls; and (5) the boundary condition of the fuel nozzle has the total pressure of 2 MPa, the velocity of 1362 m/s, and the total temperature of 1800 K (see Table 1(b)). And the fuel contains 50% of CO, 14% of H₂, and 36% of N₂.

The grid separation of the surface is shown in Figure 1(c), and the grids near the wall surface are refined

to make sure the y^+ is within the range of 1~5. And the total grid number is 2.7 million.

2.5. Case Description. Systematic simulations are conducted as shown in Table 2. The simulations are performed to investigate the effect of the chamber geometry on the combustion characteristics. In cases 1-3, the parameter H is set as constant, and the parameters A_{in} are varied. In cases 2, 4, and 5, the parameters H are varied, and A_{in} is set as constant.

2.6. Grid Independency Study and Model Validation. To make sure the grid number is suitable for the current research, the grid independency study is conducted. We use three cases with different mesh numbers, i.e., the coarse mesh with 1.9 million cells, the moderate mesh with 2.7 million, and the refined mesh with 3.8 million cells. The y_{plus} is set to 1-5 for all the cases in the independency study. The results are shown in Figure 2; as seen in the figure, the pressure variations along the axial direction of the three cases exhibit significant differences between the coarse mesh and moderate and refined mesh. Thus, to save the computational resources and maintains accuracy of the simulation, the moderate mesh is utilized for the present study.

To ensure the accuracy of the present simulation, model validation is needed. In the present research, two experimental cases are utilized, i.e., the classical DLR model proposed by Deutsches Zentrum für Luft- und Raumfahrt [21] and a ground cold flow test conducted via the connected pipe facility.

The classical DLR model is illustrated in Figure 3(a); as shown in the figure, the strut is equipped at the position marked in Figure 3(a), and the hydrogen fuel is injected into the combustor with the speed of Mach 1. The grid separation is shown in Figure 3(b).

The boundary condition of the air inlet and fuel inlet is described in Table 3; the outlet is set as pressure outlet, and the no-slip wall condition is applied for all walls in the model.

The schlieren interferogram obtained by experiment and numerical simulation is described in Figure 4. It could be seen from the figure that the expansion wave and the reflected shock wave of the simulation conform well to the experimental result. And this indicates that the proposed method can accurately predict the flow field in the ramjet combustor.

The temperatures at different axial positions are described in Figure 5; it could be seen from the figure that the trend of the temperature distribution obtained from

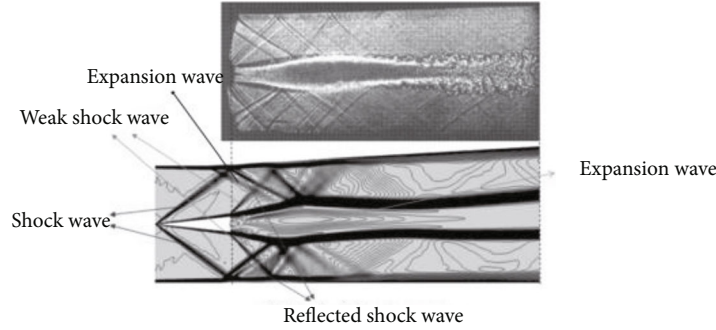


FIGURE 4: The schlieren interferogram obtained by experiment (up) and numerical simulation (down).

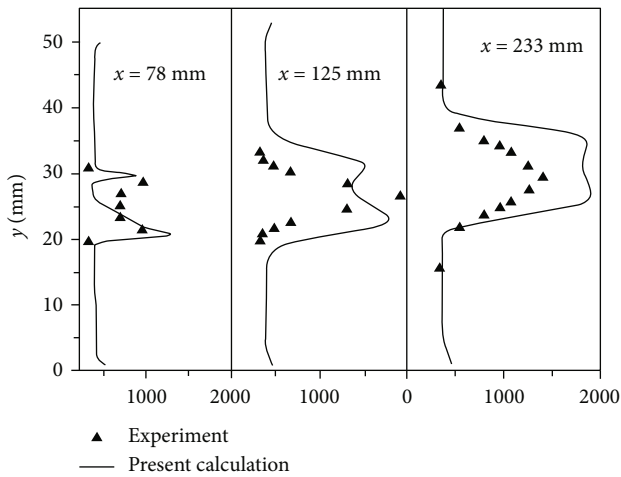


FIGURE 5: Distribution of the temperature obtained from experiment and simulation.



FIGURE 6: Scramjet engine.

TABLE 4: Experimental conditions.

Pressure (MPa)	Temperature (K)	Velocity (m/s)
1.5	650	762

the experiment and simulation is almost the same, which indicates that the proposed model can accurately predict the flow and combustion in such combustors.

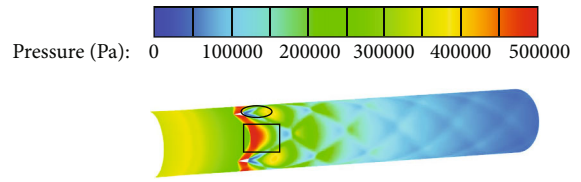


FIGURE 7: Distribution of the pressure in the chamber.

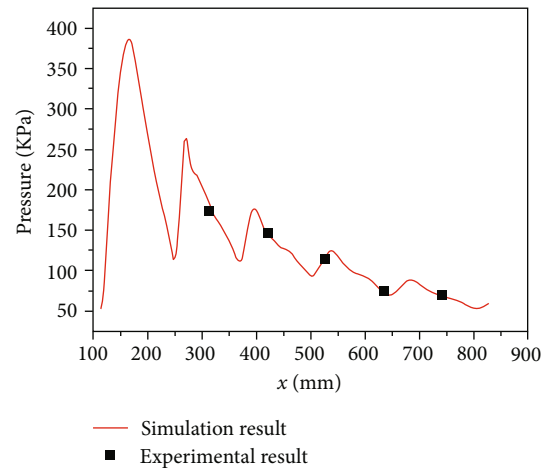


FIGURE 8: Comparison between the experimental result and numerical result.

To make sure the present model can predict the flow conditions accurately in the annular combustion chamber, a cold flow ground test is conducted via a connected pipe facility; the experimental model is almost the same as the model shown in Figure 1(b), except the parameter L_2 is 800 mm. The experimental engine is illustrated in Figure 6. Five pressure sensors are set on the engine along the axial direction, at the position of 350 mm, 450 mm, 550 mm, 650 mm, and 750 mm, with respect to the engine inlet. The experimental conditions are shown in Table 4.

As for the simulation part, the boundary condition is the same as described in Section 2.4 (Figure 2), and the physical model is the same as the experimental one. The result is shown in Figure 7. In this figure, the distribution of the pressure field is illustrated; unlike the flow patterns shown in

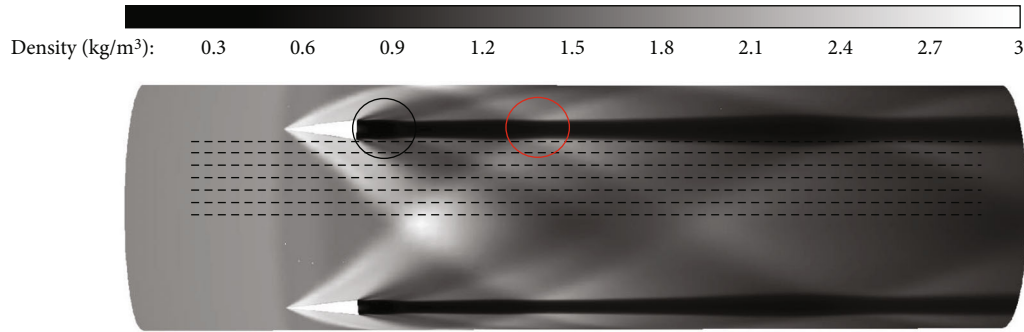


FIGURE 9: The distribution of the density at the surface of $r = 50$ mm.

Figure 3, in an annular flow field, the shock wave is mainly dominated by the strut placed along the circumferential direction, rather than the combustor wall. Thus, this may lead to the phenomena occurring in the middle of the two struts (marked with the square), and the cells with diamond shapes appear downstream of the flow field. In addition, it is worth noting that the low pressure region with the shape of a swallowtail could be observed at the bottom of the struts (as marked with the circle).

The results obtained from the experiment and simulation are shown in Figure 8; it is worth noting that the results obtained from the simulation reveal a wave shape; this is believed to be caused by the abovementioned diamond-shaped pressure distribution. And it can also be seen that the pressure measured at the measuring points conforms well to the simulation result, which means that the proposed method can accurately predict the flow patterns in the combustor.

3. Results and Discussion

3.1. Flow-Field Characteristics. In this section, case 2 is used to investigate the mixing characteristics of the combustor, without ignition. The distribution of the density is shown in Figure 9; as described in this figure, an oblique shock wave is generated at the tip of the strut and gets crossed to another shock wave formed at the other strut, as marked with the square. The two-crossed shock waves are further extended to the shear layer generated by the fuel and incoming air and then reflected, which eventually leads to the cell with a diamond shape. It is worth noting that there are some weak shock waves generated at the end of the strut (marked with a circle), which is the same as the oblique shock wave; these weak shock waves are also crossed and reflected with each other and the shear layer.

The distributions of the density at the ISO surfaces parallel to the XOY plane between the two struts (as marked by the dashed line in Figure 9) are illustrated in Figure 10; as shown in the figure, the shock wave feature is mainly dominated by the strut. And at the position where the oblique shock wave is generated, the boundary layer becomes thicker (as marked by the square), and at the bottom of the strut, the density distribution shows a little discontinued behavior (as marked by the circle); this is believed to be caused by the weak shock wave mentioned above.

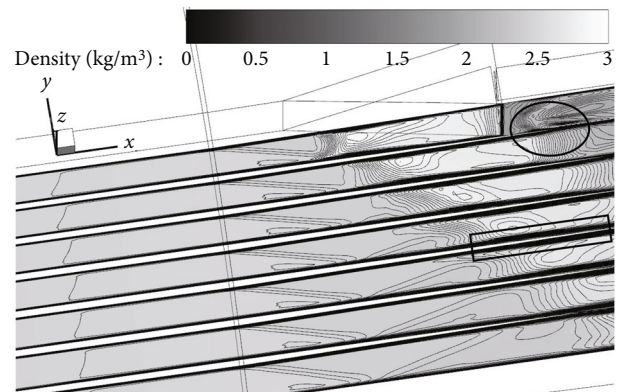
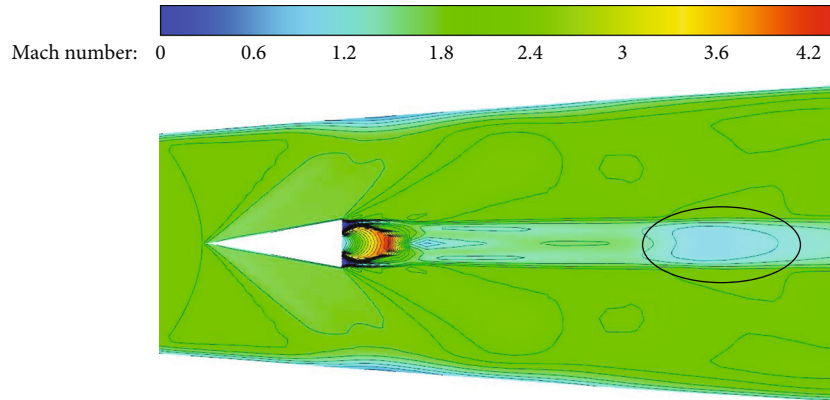


FIGURE 10: The density distribution of different surface parallel to the XZ plane.

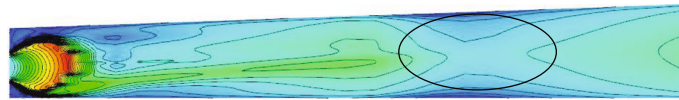
The distribution of the Mach number and static pressure is illustrated in Figures 11 and 12. It could be seen from Figure 11(a) that the velocity of the fuel increased rapidly near the fuel inlet and then decreases gradually downstream the flow field; and at the position marked by the circle (corresponding to the marked location at Figure 11(b)), the velocity goes even lower, which is mainly owing to the crossed shock wave. As described in Figure 12, a region with high speed and low pressure occurs around the bottom of the strut, owing to the expended jet flow at the fuel inlet; as the jet flow develops downstream, the pressure goes higher and becomes steady gradually.

The temperature distribution is shown in Figure 13; the temperature decreases rapidly near the bottom of the strut and increases gradually downstream the flow field. It is noticed that the high-temperature zone mainly occurs around the center of the jet flow and could be significantly affected by the distribution of the shock wave (see Figure 13(a)). In addition, as shown in Figure 13(b), the temperature goes higher near the wall; this is believed to be caused by the crossing and reflecting effects of the shock wave, which reminds us that more attention should be paid to the thermal protection in this area.

3.2. Mixing Characteristics. Figures 14 and 15 illustrate the distribution of the mass fraction of CO and H₂. As shown



(a) Distribution of the Mach number at the surface of $z = 50$ mm



(b) Distribution of the Mach number at the surface of $y = 0$ mm

FIGURE 11: Distribution of the Mach number.

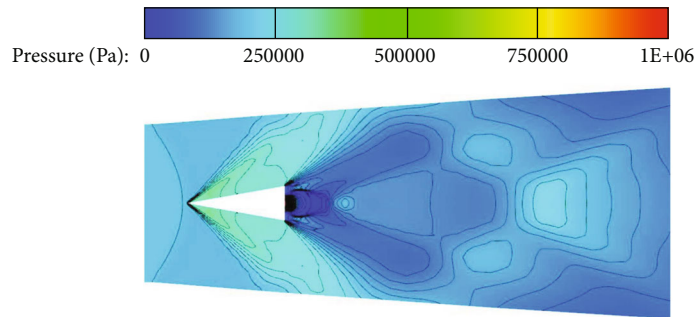
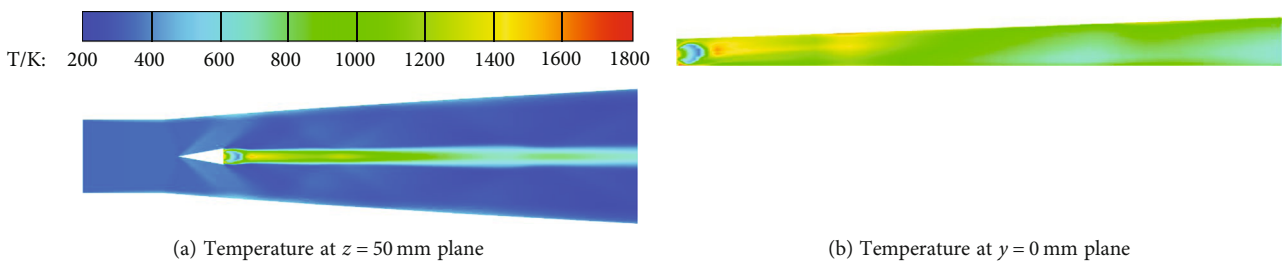


FIGURE 12: Distribution of pressure.



(a) Temperature at $z = 50$ mm plane

(b) Temperature at $y = 0$ mm plane

FIGURE 13: Distribution of temperature.

in those figures, the mass fraction of gases goes higher near the fuel inlet and decreases gradually as the jet flow developed. And the gases are all concentrated in the shear layer owing to the characteristics of the jet flow (see Figures 14(a) and 15(a)). As shown in Figures 14(b) and 15(b), in the view of $y = 0$ mm plane, the jet flow goes up near the wall, and this is believed to be caused by the asymmetric expansion of the combustor.

To analyze the mixing characteristic more clearly, the mixing coefficient is calculated, which could be obtained

via [26]

$$\eta_{\text{mix}} = \frac{\int_A \alpha \rho u Y_{\text{fuel}} dA}{\dot{m}_{\text{fuel}}}, \quad (11)$$

where ρ is the density of the mixture, u is normal velocity, Y_{fuel} represents the mass fraction of the fuel, A is the area of the ISO surface of the combustor, \dot{m}_{fuel} means the mass

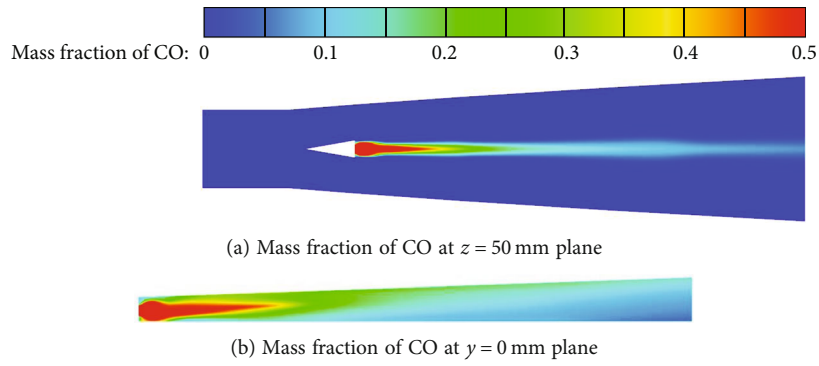


FIGURE 14: Distribution of mass fraction of CO.

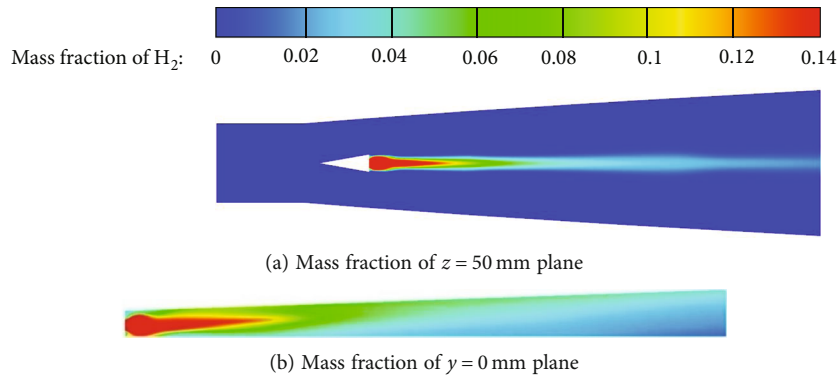


FIGURE 15: Distribution of mass fraction of H_2 .

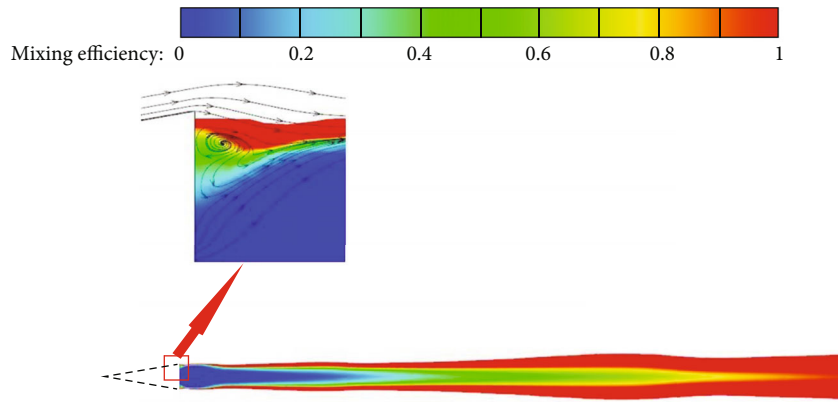


FIGURE 16: The mixing efficiency at the plane of $z = 50$ mm.

flux of the fuel, and α is the residual gas coefficient, regarded as the inverse of the equivalence ratio (Φ). And the equivalence ratio (Φ) could be calculated via

$$\phi = \frac{8Y_{H_2} + ((4/7)Y_{CO})}{Y_{O_2}}. \quad (12)$$

The residual gas coefficient α is defined as

$$\alpha = \begin{cases} 1, & \phi < 1, \\ 1/\phi, & \phi \geq 1. \end{cases} \quad (13)$$

The mixing efficiency at the plane of $z = 50$ mm is

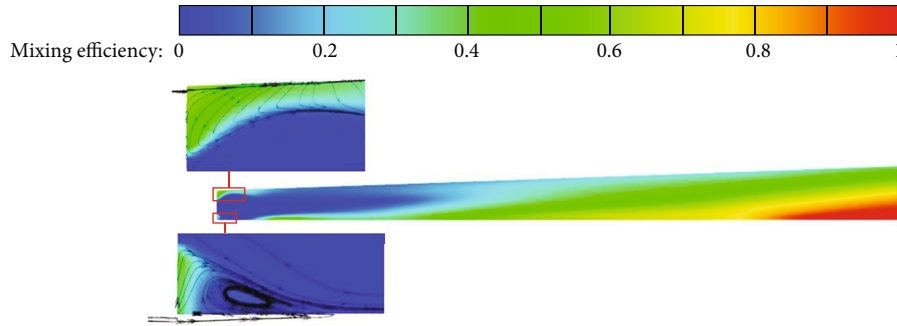


FIGURE 17: The mixing efficiency at the plane of $y = 0$.

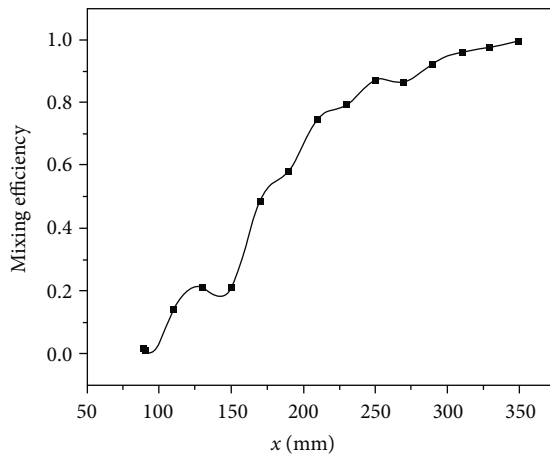


FIGURE 18: The mixing efficiency at the axis of $y = 0$ mm and $z = 50$ mm plane.

illustrated in Figure 16; it could be seen from the figure that the mixing coefficient reaches the highest value at the location of the shear layer between the jet flow and incoming air. And as the jet flow moves downstream, the mixing coefficient goes higher. It could be also seen from the zoom in view of Figure 16, at the area of the recirculation zone, that the mixing coefficient is increased, which indicates that the mixing coefficient could be enhanced under the effect of the recirculated flow.

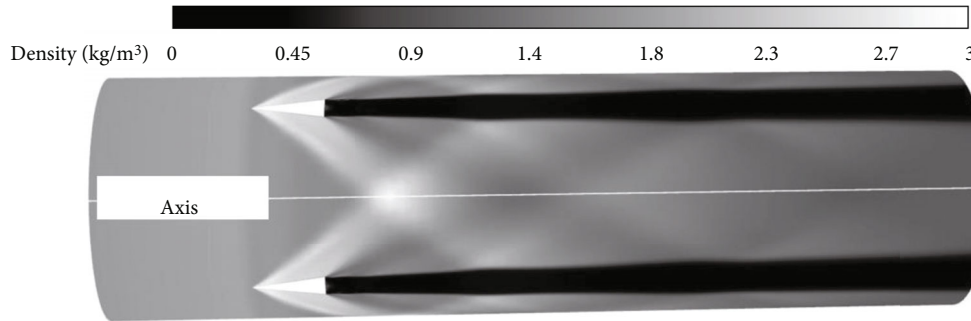
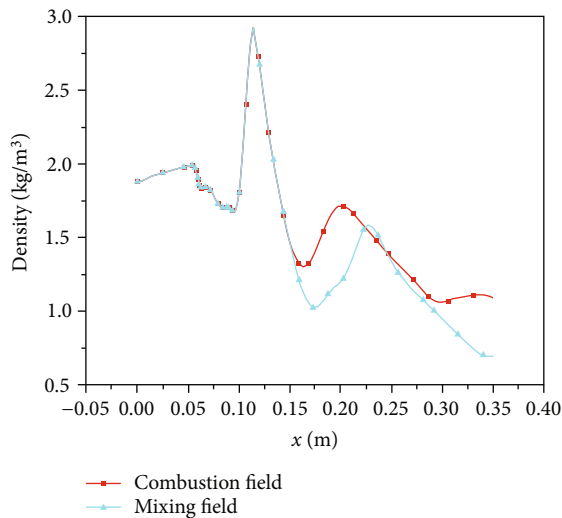
Figure 17 illustrates the mixing coefficient at $y = 0$ mm plane. It could be observed from the figure that the mixing coefficient is increased as the fuel jet flow develops downstream, and the mixing coefficient at the lower wall of the combustor is higher than that of the upper wall. It could be also observed from the zoom in view of the figure that the mixing coefficient near the bottom of the strut is lower than that of $z = 50$ mm plane. The reason behind is that the location is close to the combustor wall; this may not lead to a fully developed recirculation zone, which further leads to a decrease in the mixing coefficient.

The distribution of the mixing coefficient is described in Figure 18; the profile is obtained at the axis of $y = 0$ mm and $z = 50$ mm plane. It is noticed that at 75-150 mm, the mixing coefficient increases gradually, corresponding to the location of the core area of the jet flow; in this area, the diffusion

effect is not quite significant, and the increase of the mixing coefficient is mainly owing to the weak shock waves at the bottom of the strut (see Figure 9 marked by the black circle). And at the range of 150 mm, the mixing coefficient increases rapidly; this is believed to be caused by the crossed shock wave shown in Figure 9 (marked by the red circle); the shock wave here can reduce the velocity of the jet flow and on the other hand enhance the mixing coefficient. It is worth noting that at the range of 125 mm-150 mm, the mixing coefficient decrease a little; this is mainly caused by the developed jet flow between the weak shock waves and the crossed shock wave (see the range between the black circle and red circle in Figure 9); in this range, the jet flow developed sufficiently without the disturbance of the shock wave, which leads to a decrease in the mixing coefficient on some level. After this, at the location of 275 mm, the mixing coefficient increased further; this is also corresponding to the location of the crossed shock wave, which indicates that the velocity is further reduced. It could be seen from the figure that the overall trend increased and reached its maximum at the outlet of the combustor, but an upward trend could still be observed at the outlet of the combustor; thus, an assumption could be made that if the length of the combustor is increased, the mixing coefficient could be further enhanced up to 100%.

3.3. Combustion Characteristics. In this section, the ignition is started to analyze the combustion characteristics of the present annular combustor. The distribution of the density is illustrated in Figure 19; compared to the density of the noncombusted result shown in Figure 9, the overall trends are almost the same, except for the thickness of the jet flow.

To analyze the density distribution in detail, the density along the axis (marked in Figure 19) is obtained and compared with that of the noncombusted result. As shown in Figure 20, in the part of the isolator (0-100 mm) and the head of the extension region (100-125 mm), the densities are the same, owing to the combustion that is not involved in such region. However, for the regions where the combustion occurs (>125 mm), the density distribution shows few differences. It is worth to be noticed that the peaks described in Figure 20 conform to the location where the shock waves are crossed, and the locations of the shock wave crossing point of the two cases are the same, while at the second point around the location of 200 mm, a significant gap could be observed between the two cases. This indicates that the

FIGURE 19: Density distribution of the surface at $r = 50$ mm.FIGURE 20: The density distribution at the axis of $y = 0$ mm and $z = 50$ mm plane.

combustion may lead to some changes in the structures of the shock waves. And it could be seen from Figure 20 that the overall trend of the density for the combustion cases is higher than that of the noncombusted case; this is mainly caused by the combustion of the CO and H₂; the products of those two working mediums may enhance the total density of the flow fields.

Figures 21 and 22 illustrate the distribution of the reacting species (CO, CO₂, and O₂). The distribution of H₂ is almost the same as that of CO; thus, the distribution of H₂ is not provided. The mass fraction of CO is decreased as the fuel jet flow is developed, and this is mainly owing to the increase in the mass fraction of combustion products (see Figure 21). As shown in $z = 50$ mm plane of Figures 20 and 21, the combustion mainly occurs in the shear layer, strut bottom, and downstream the flow field; this corresponds to the results shown in Figure 16; the combustion occurs where the high mixing efficiency is obtained; thus, it could be concluded that the higher mixing rate can result in efficient combustion.

The distribution of the temperature is shown in Figure 23; the high temperature zone shows a cylindrical shape and expands as the jet flow developed. It could be seen

that the higher temperature could be obtained at the shear layer and the recirculation zone near the bottom of the strut; the temperature at the shear layer can reach over 2400 K, and the temperature at bottom of the strut is higher than 2600 K. These regions are often regarded as the flame surface.

The heat of reaction is shown in Figure 24; combined with the temperature distribution described above, the heat release at the flame surface is highest overall. And at the bottom of the strut, the heat release reaches the maximum and decreases gradually downstream of the flow field. It is worth noting that the heat release and temperature inside the jet flow are much lower than that of the flame surface. As described in Ref. [42], the flame surface is often regarded as the interface of the oxide rich region (outside the flame surface) and fuel rich region (inside the flame surface); the combustion inside the flame surface is mainly dominated by the chemical process; the combustion at the shear layer is controlled by diffusion process. In the diffusion process-controlled regions, i.e., the flame surface, the combustion occurs in stoichiometric ratio; thus, this may lead to a higher temperature and heat release rate in such region.

The combustion efficiency is a key factor that can evaluate the combustion performance, which could be calculated via

$$\eta_i = 1 - \frac{\int \rho Y_i u dA}{\dot{m}_{i,\text{in}}} = 1 - \frac{\dot{m}_{i,A}}{\dot{m}_{i,\text{in}}}, \quad (14)$$

where η_i is the local combustion efficiency, Y_i represents the local mass fraction, $\dot{m}_{i,\text{in}}$ and $\dot{m}_{i,A}$ are the initial mass flow rate and present mass flow rate at a certain surface, and the subscript i means the i^{th} component.

Based on the abovementioned equation, the combustion efficiency at the certain surface A could be defined as below:

$$\eta_{\text{fuel}} = 1 - \frac{\sum_i \dot{m}_{i,A}}{\sum_i \dot{m}_{i,\text{in}}}, \quad (15)$$

The combustion efficiency is illustrated in Figure 25; in this figure, the combustion efficiency is obtained at the axis defined by the surface of $z = 50$ mm (XOY) and $y = 0$ mm (XOZ). It could be seen from the figure that the overall trend of the combustion efficiency is increased downstream, and at the exit of the combustor, the combustion efficiency of H₂ is

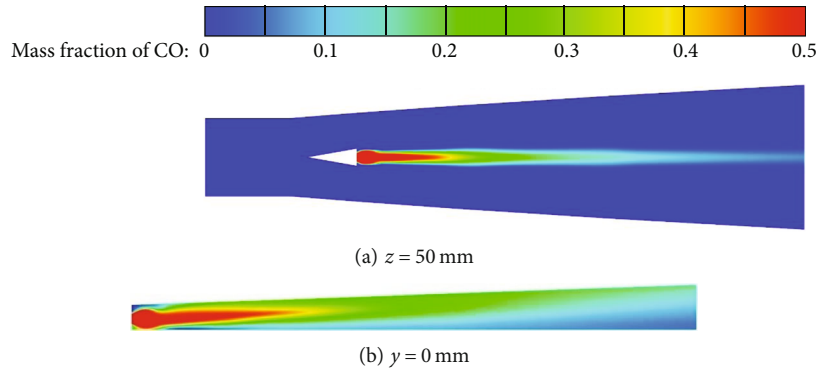


FIGURE 21: Distribution of mass fraction of CO.

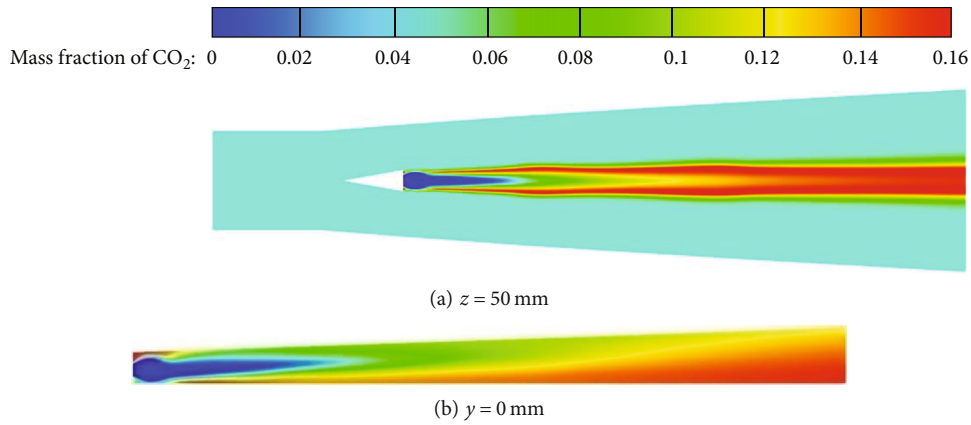


FIGURE 22: Distribution of mass fraction of CO₂.

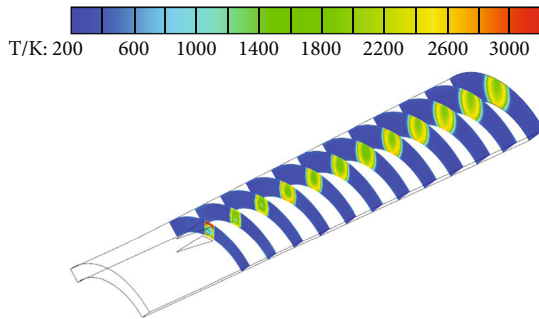


FIGURE 23: Distribution of temperature.

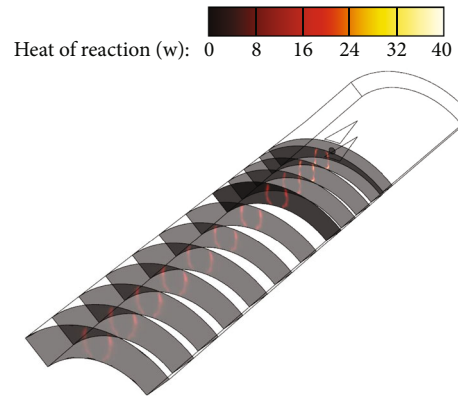


FIGURE 24: Distribution of combustion heat release rate.

48.9% and CO is 61.4%, and the total combustion efficiency is 58.7%. It is worth noting that at the location around 80 mm, η_{fuel} is 0; this is corresponding to the phenomena described in Figures 14 and 15; in this area, the mass fraction of the fuel is almost 100%; thus, no combustion could be established under such condition.

3.4. The Effect of Combustion Characteristics in the Chamber Geometry. The mixing efficiency for different cases is illustrated in Figures 26 and 27. As shown in Figure 26, the overall trend of the mixing efficiency is increased with the decrease of the A_{in} (see cases 1, 2, and 3), and they are all fully mixed at the outlet of the combustor. It is worth to be noticed that as A_{in} is

decreased, the location where the mixing efficiency reaches 100% moves upstream of the flow field. As for the cases with different H (see cases 4, 2, and 5 in Figure 26), the mixing efficiency is increased with the increased value of H , and it is the same as the cases mentioned above; as the H is increased, the location of the 100% mixing efficiency moves towards the inlet of the combustor. It should be particularly noticed that as shown in case 4 of Figure 26, the fuel gas is not fully mixed even at the outlet of the combustor, which indicates that an

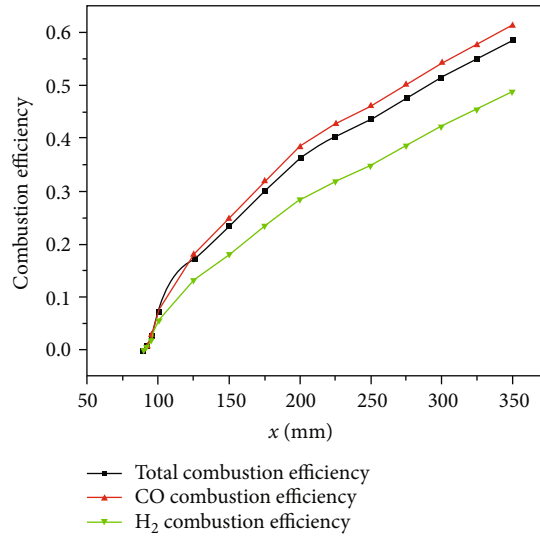


FIGURE 25: Combustion efficiency.

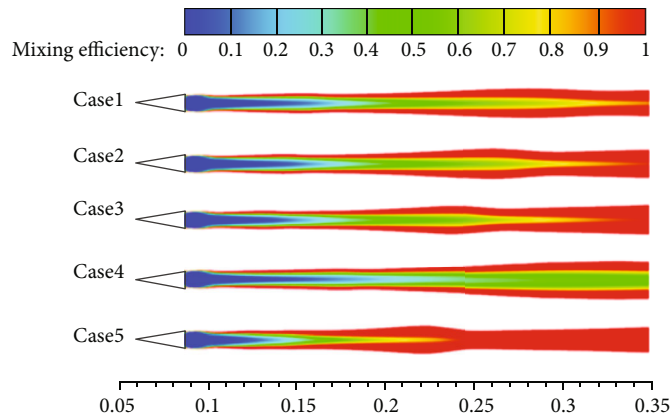


FIGURE 26: Mixing efficiency for different cases.

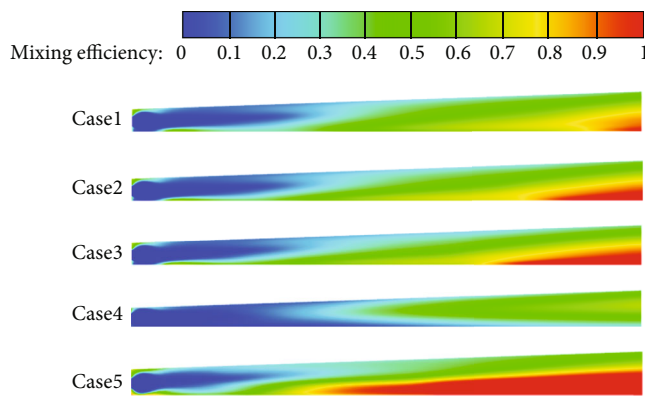


FIGURE 27: Mixing efficiency for different cases at $y = 0$ mm plane.

overnarrow path of the annular combustor may negatively affect the mixing characteristics of the combustor.

Figure 27 illustrates the mixing efficiency of XOY plane at the position of $y = 0$ mm. As shown in the figure, the mixing efficiency has the same trend compared to the result shown in Figure 26. It is worth to be noticed that case 4

expresses a poor mixing efficiency, and this is believed to be caused by the nonfully expanded structure of the combustor.

As mentioned above, the mixing efficiency is related to the structure of the shock wave; thus, the analysis based on the structure of the shock wave is presented. As described

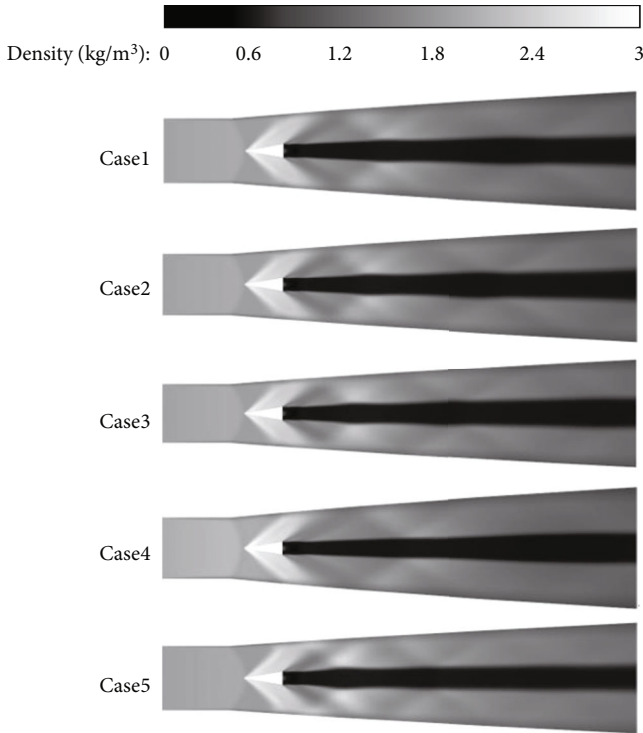


FIGURE 28: Density distribution for different cases.

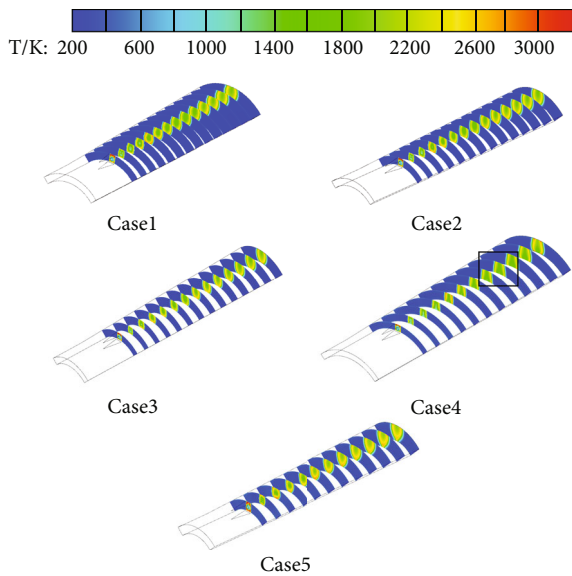


FIGURE 29: The temperature distribution for cases 1-5.

in Figure 28, the shock waves are crossed at the center of the jet flow for all the cases. However, the location of the crossing point is not the same. As for cases 1, 2, and 3, the crossing point near the bottom of the nozzle moves upstream as the inlet area is decreased; this is mainly owing to the decreasing of the angle between the shock wave and the strut as A_{in} is decreased. As described in Figure 28 cases 4, 2, and 5, the increase in H may lead to the increased angle between

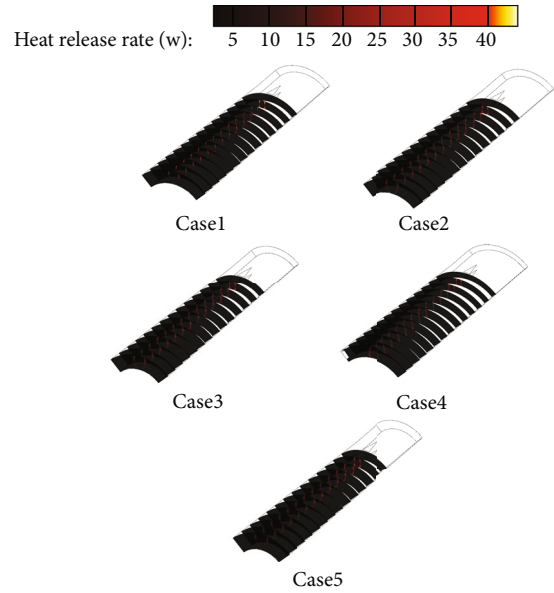


FIGURE 30: The heat release distribution for cases 1-5.

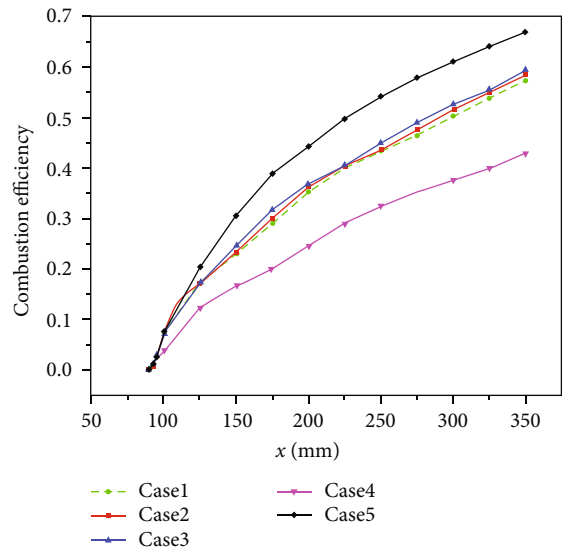


FIGURE 31: The distribution of the combustion efficiency for different cases.

the shock wave and the strut, which further makes the crossed point move upstream. And those phenomena eventually lead to the difference in the mixing efficiency.

The temperatures for each case are illustrated in Figure 29; it could be seen from the figure, in cases 1-3, that the distribution of the temperature is almost the same, and the high-temperature zone is mainly concentrated on the surface of the lower wall. However, as shown in cases 4, 2, and 5, the temperature distributions are quite different; as for the case with the smallest H , the flame surface with the highest temperature expressed a trapezoid shape

TABLE 5: Combustion efficiency at the exit of the combustor.

Case	Case 1	Case 2	Case 3	Case 4	Case 5
Combustion efficiency (%)	57.393	58.687	59.531	42.962	67.164

downstream of the flow field. And the flame surface temperature in the middle of the expansion region reaches 2400 K, which is lower than that of the cases with higher H . As for cases 2 and 5, the shape of the flame surface expressed an inverted triangle shape.

The distributions of heat release rate are shown in Figure 30; the heat release rate is often used to describe the shape of the flame, and as shown in the figure, the flame shape expresses an inverted triangle shape in cases 1, 2, and 3. And the heat release is higher at the inlet of the fuel, which means that the combustion near the bottom of the strut is more sufficient; this further confirmed that the recirculation zone at the strut bottom has a positive effect on the combustion. It could be seen from cases 1, 2, and 3 that the heat release rate gets much lower compared to that of the fuel inlet; this is mainly owing to the reduction of the mass fraction of the fuel gas. And it is worth to be noticed that the heat release downstream in case 1 is a little lower than that of cases 2 and 3, which implies that the decreasing of the inlet area can enhance the heat release of the expansion region.

As shown in cases 4, 2, and 5 of Figure 30, in case 4, the flame shape expresses a trapezoid shape; this is mainly dominated by the narrow path of the annular combustor; the distance between the upper and lower wall is too small, and the combusted jet flow is not fully developed. As the diameter of the path is increased (shown in cases 2 and 5), the inverted triangle shape appears downstream of the chamber; this means that the jet flow is fully developed with a larger path size. And as the size of the path is increased, the bottom tip of the inverted triangle flame moves away from the lower wall of the combustor.

The combustion efficiency is shown in Figure 31 and Table 5; it could be seen from the figure and table that the combustion efficiency increases as the inlet area is decreased, but the overall trend is almost the same, which implies that the variation of the inlet area has an insignificant effect of the combustion efficiency. However, for cases 4, 2, and 5, the combustion efficiency could be significantly enhanced as the height of the path is increased. This partially indicates that the combustion efficiency could be enhanced when the connected area between gas and air is increased.

As described in the paper [26, 43], the authors use three different configurations of the strut, i.e., single strut, double strut, and double struts with backward-facing steps. It could be observed that the combustion efficiency for single strut case is around 70% and for double strut case is almost 90%, and for the cases with backward-facing step struts, the combustion efficiency is larger than 90%. In our cases, the maximum combustion efficiency occurs in case 5 with the value of 67%, which is obviously lower than that of the double and backward-facing step struts and a little lower than that of single strut case. However, it is worth noting that the DLR engine utilized in the above-

mentioned references is fueled by hydrogen only, while in the present research, the CO and H_2 mixture is applied as gaseous fuel, and the mass fraction of CO is much higher than H_2 , and the diffusion rate of H_2 ($1.29 \text{ cm}^2/\text{s}$ at 300 K and 101325 Pa) is much higher than that of CO ($0.175 \text{ cm}^2/\text{s}$ at 300 K and 101325 Pa) in air; thus, this may lead to the lower combustion efficiency in the current engine structure. In addition, the abovementioned research is based on the DLR-type combustor, and the practical application is difficult to achieve; however, the annular strut-based combustor in this article offers the possibility of engineering application use. And it is worth to be noticed that the double and backward-facing step struts can significantly improve the combustion efficiency of the engine; this offers us an idea that the combustion efficiency could be improved via changing the strut configuration, and this will be the upcoming research of the project.

4. Conclusion

In this work, a new configuration of the strut-based scramjet is proposed, and a series of simulations are conducted. The effects of the geometry of the combustor in such scramjets are investigated and analyzed. The key conclusions are summarized as

- (i) The flow field of present engine shows the same characteristics as the classical DLR engine. The oblique shock wave is generated at the tip of the strut and gets crossed to another shock wave formed at the other strut. And the fuel jet flow goes up near the upper wall of the combustor, which is believed to be caused by the asymmetric expansion of the combustor
- (ii) The investigation of the mixing characteristics indicates that the recirculation zone near the bottom tip of the strut can increase the mixing coefficient. And at the range 150 mm and 170 mm, the mixing coefficient increases rapidly; the reason behind that is the crossed shock wave; the shock wave here can reduce the velocity of the jet flow and on the other hand enhance the mixing coefficient
- (iii) The research on the combustion field indicates that the temperature is higher near the shear layer and the strut bottom; the temperature at the shear layer can reach over 2400 K, and the temperature at bottom of the strut is higher than 2600 K. These regions are often regarded as the flame surface
- (iv) Increasing A_{in} can lead to an increase in the overall trend of the mixing efficiency and reduce the combustion heat release rate and combustion efficiency. However, the case with the narrowest H expresses

the poorest mixing characteristics and significantly affects the combustion efficiency. And the flame shape could be sensitive to the chamber geometry

In general, the present work proposes a new geometry of the scramjet combustor, and the feasibility of such combustors is investigated via numerical approach. The results indicate that the application for such combustors is possible, but further investigation is still needed.

Nomenclature

Q :	Conservative vectors
E :	Convective flux vectors
F :	Convective flux vectors
E_V :	Viscous flux vectors
F_V :	Viscous flux vectors
H :	Convective flux vectors
H_V :	Viscous flux vectors
S :	Source term produced by chemical reaction
ρ :	Total density (kg/m^3)
u :	Axial velocity (m/s)
v :	Radial velocity (m/s)
w :	Tangential velocity (m/s)
E :	Energy (J)
p :	Pressure (Pa)
τ :	Shear stress (Pa)
q :	Heat fluxes (W/m^2)
μ :	Total viscosity (Pa·s)
μ_i :	Laminar viscosity (Pa·s)
μ_t :	Turbulent viscosity (Pa·s)
T :	Temperature (K)
λ :	Thermal conductivity ($\text{W}/(\text{m}\cdot\text{K})$)
D_i :	Diffusion coefficient for component i (m^2/s)
m_i :	Mass source for component i
c_i :	Mass fraction for component i
ρ_i :	Density for component i (kg/m^3)
h_i :	Enthalpy of unit mass for component i (J/kg)
Sc :	Laminar Schmidt number
Sct :	Turbulent Schmidt number
X_i :	Mole fraction of component i
X_j :	Mole fraction of component j
μ_{li} :	Laminar viscosity of components i (Pa·s)
μ_{lj} :	Laminar viscosity of components j (Pa·s)
M_i :	Molecular weight of components i (kg/mol)
M_j :	Molecular weight of components j (kg/mol)
P_{rl} :	Laminar Prandtl numbers
P_{rt} :	Turbulent Prandtl numbers
c_p :	Specific heat at constant pressure (J/(kg·K))
R_u :	Universal gas constant ($\text{J}\cdot\text{mol}^{-1}\cdot\text{K}^{-1}$)
h_i^{298} :	Heat of formation of component i (J/kg)
C_{pi} :	Specific heat at constant pressure of component i (J/(kg·K))
η_{mix} :	Mixing coefficient
Φ :	Equivalence ratio
α :	Residual gas coefficient
η_{fuel} :	Combustion efficiency
$\dot{m}_{i,\text{in}}$:	Initial mass flow rate at a certain surface (kg/s)

$\dot{m}_{i,A}$: Present mass flow rate at a certain surface (kg/s)

Subscripts

x : x direction
 y : y direction
 z : z direction

Data Availability

All the data used to support the findings of this study are available from the corresponding author upon request.

Conflicts of Interest

The authors declare that they have no conflict of interest.

Acknowledgments

The authors would like to acknowledge the financial support from the National Natural Science Foundation of China (52006099).

References

- [1] J. Urzay, "Supersonic combustion in air-breathing propulsion systems for hypersonic flight," *Annual Review of Fluid Mechanics*, vol. 50, no. 1, pp. 593–627, 2018.
- [2] D. J. Micka and J. F. Driscoll, "Combustion characteristics of a dual-mode scramjet combustor with cavity flameholder," *Proceedings of the Combustion Institute*, vol. 32, no. 2, pp. 2397–2404, 2009.
- [3] K.-Y. Hsu, C. D. Carter, M. R. Gruber, T. Barhorst, and S. Smith, "Experimental study of cavity-strut combustion in supersonic flow," *Journal of Propulsion and Power*, vol. 26, no. 6, pp. 1237–1246, 2010.
- [4] C.-H. Kim, I.-S. Jeung, B. Choi, T. Kouchi, K. Takita, and G. Masuya, "Effect of fuel injection location on a plasma jet assisted combustion with a backward-facing step," *Proceedings of the Combustion Institute*, vol. 33, no. 2, pp. 2375–2382, 2011.
- [5] W. Huang and L. Yan, "Numerical investigation on the ram-scram transition mechanism in a strut-based dual-mode scramjet combustor," *International Journal of Hydrogen Energy*, vol. 41, no. 8, pp. 4799–4807, 2016.
- [6] H. Wang, Z. Wang, M. Sun, and H. Wu, "Combustion modes of hydrogen jet combustion in a cavity-based supersonic combustor," *International Journal of Hydrogen Energy*, vol. 38, no. 27, pp. 12078–12089, 2013.
- [7] H. Wang, Z. Wang, M. Sun, and N. Qin, "Large eddy simulation of a hydrogen-fueled scramjet combustor with dual cavity," *Acta Astronautica*, vol. 108, pp. 119–128, 2015.
- [8] W. Huang, M. Pourkashanian, L. Ma, D. B. Ingham, S. Luo, and Z. Wang, "Effect of geometric parameters on the drag of the cavity flameholder based on the variance analysis method," *Aerospace Science and Technology*, vol. 21, no. 1, pp. 24–30, 2012.
- [9] J. W. Kirik, C. P. Goynes, S. J. Peltier, C. D. Carter, and M. A. Hagenmaier, "Velocimetry measurements of a scramjet cavity flameholder with inlet distortion," *Journal of Propulsion and Power*, vol. 30, no. 6, pp. 1568–1576, 2014.

- [10] T. Ombrello, S. Peltier, and C. D. Carter, "Effects of inlet distortion on cavity ignition in supersonic flow," in *53rd AIAA Aerospace Sciences Meeting*, p. 882, Kissimmee, Florida, 2015.
- [11] O. R. Kummitha, K. M. Pandey, and R. Gupta, "Numerical analysis of hydrogen fueled scramjet combustor with innovative designs of strut injector," *International Journal of Hydrogen Energy*, vol. 45, no. 25, pp. 13659–13671, 2020.
- [12] Z. Gao and C. Lee, "A numerical study of turbulent combustion characteristics in a combustion chamber of a scramjet engine," *SCIENCE CHINA Technological Sciences*, vol. 53, no. 8, pp. 2111–2121, 2010.
- [13] M.-B. Sun, Z.-G. Wang, J.-H. Liang, and H. Geng, "Flame characteristics in supersonic combustor with hydrogen injection upstream of cavity flameholder," *Journal of Propulsion and Power*, vol. 24, no. 4, pp. 688–696, 2008.
- [14] W. Huang, W. Liu, S. Li, Z. Xia, J. Liu, and Z. Wang, "Influences of the turbulence model and the slot width on the transverse slot injection flow field in supersonic flows," *Acta Astronautica*, vol. 73, pp. 1–9, 2012.
- [15] H. Wang, M. Sun, N. Qin, H. Wu, and Z. Wang, "Characteristics of oscillations in supersonic open cavity flows," *Flow, Turbulence and Combustion*, vol. 90, no. 1, pp. 121–142, 2013.
- [16] W. Huang, "Investigation on the effect of strut configurations and locations on the combustion performance of a typical scramjet combustor," *Journal of Mechanical Science and Technology*, vol. 29, no. 12, pp. 5485–5496, 2015.
- [17] L. Biao, Z. Wei, and H. Chi, "Numerical analysis of solid fuel scramjet operating at Mach 4 to 6," in *49th AIAA/ASME/SAE/ASEE Jt. Propulsion Conference*, p. 3695, San Jose, CA, 2013.
- [18] H. Chi, Z. Wei, L. Wang, B. Li, and Z. Wu, "Numerical investigation of self-ignition characteristics of solid-fuel scramjet combustor," *Journal of Propulsion and Power*, vol. 31, no. 4, pp. 1019–1032, 2015.
- [19] L. Wang, S. Li, H. Chi, B. Li, Z. Wei, and N. Wang, "Quasi-one-dimensional numerical method for solid fuel scramjet combustor analysis and design," *Journal of Aerospace Engineering*, vol. 28, no. 3, p. 4014083, 2015.
- [20] H. Tao and Z. Wei, "Numerical investigation on the effects of cavity in solid fuel scramjet," in *49th AIAA/ASME/SAE/ASEE Jt. Propulsion Conference*, p. 3974, San Jose, CA, 2013.
- [21] W. Waidmann, F. Alff, M. Böhm, U. Brummund, W. Clauss, and M. Oswald, "Supersonic combustion of hydrogen/air in a scramjet combustion chamber," *Space Technology*, vol. 15, pp. 421–429, 1995.
- [22] V. A. Vinogradov, S. A. Kobigsky, and M. D. Petrov, "Experimental investigation of kerosene fuel combustion in supersonic flow," *Journal of Propulsion and Power*, vol. 11, no. 1, pp. 130–134, 1995.
- [23] M. A. Witt, *Investigation into the Feasibility of Using Solid Fuel Ramjets for High Supersonic/Low Hypersonic Tactical Missiles*, Naval Postgraduate School Monterey CA, 1989.
- [24] W. J. Angus, *An Investigation into the Performance Characteristics of a Solid Fuel Scramjet Propulsion Device*, Postgraduate School Monterey CA, NAVAl, 1991.
- [25] E. T. Curran and S. N. B. Murthy, *Scramjet propulsion*, AIAA, 2001.
- [26] C. Li, X. Chen, Y. Li, O. Musa, and L. Zhu, "Numerical investigation on the performance of scramjet combustor with a novel strut configuration," *Applied Thermal Engineering*, vol. 159, article 113894, 2019.
- [27] C. Li, Z. Xia, L. Ma, X. Zhao, and B. Chen, "Experimental and numerical study of solid rocket scramjet combustor equipped with combined cavity and strut device," *Acta Astronautica*, vol. 162, pp. 145–154, 2019.
- [28] C. Li, Z. Xia, L. Ma, X. Zhao, and B. Chen, "Numerical study on the solid fuel rocket scramjet combustor with cavity," *Energies*, vol. 12, no. 7, p. 1235, 2019.
- [29] X. Pei and L. Hou, "Numerical investigation on cavity structure of solid-fuel scramjet combustor," *Acta Astronautica*, vol. 105, no. 2, pp. 463–475, 2014.
- [30] P. Yang, Z. Xia, L. Ma et al., "Influence of the multicavity shape on the solid scramjet," *International Journal of Aerospace Engineering*, vol. 2021, Article ID 9718537, 2021.
- [31] M. B. Sun, C. Gong, S. P. Zhang, J. H. Liang, W. D. Liu, and Z. G. Wang, "Spark ignition process in a scramjet combustor fueled by hydrogen and equipped with multi-cavities at Mach 4 flight condition," *Experimental Thermal and Fluid Science*, vol. 43, pp. 90–96, 2012.
- [32] O. R. Kummitha, "Numerical analysis of hydrogen fuel scramjet combustor with turbulence development inserts and with different turbulence models," *International Journal of Hydrogen Energy*, vol. 42, no. 9, pp. 6360–6368, 2017.
- [33] O. R. Kummitha, "Numerical analysis of passive techniques for optimizing the performance of scramjet combustor," *International Journal of Hydrogen Energy*, vol. 42, no. 15, pp. 10455–10465, 2017.
- [34] O. R. Kummitha, L. Suneetha, and K. M. Pandey, "Numerical analysis of scramjet combustor with innovative strut and fuel injection techniques," *International Journal of Hydrogen Energy*, vol. 42, no. 15, pp. 10524–10535, 2017.
- [35] G. Choubey and K. M. Pandey, "Effect of variation of angle of attack on the performance of two-strut scramjet combustor," *International Journal of Hydrogen Energy*, vol. 41, no. 26, pp. 11455–11470, 2016.
- [36] K. M. Pandey, S. Roga, and G. Choubey, "Numerical investigation on hydrogen-fueled scramjet combustor with parallel strut fuel injector at a flight Mach number of 6," *Journal of Applied Fluid Mechanics*, vol. 9, no. 3, pp. 1215–1220, 2016.
- [37] G. Choubey and K. M. Pandey, "Effect of different wall injection schemes on the flow-field of hydrogen fuelled strut-based scramjet combustor," *Acta Astronautica*, vol. 145, pp. 93–104, 2018.
- [38] G. Choubey and K. M. Pandey, "Effect of parametric variation of strut layout and position on the performance of a typical two-strut based scramjet combustor," *International Journal of Hydrogen Energy*, vol. 42, no. 15, pp. 10485–10500, 2017.
- [39] P. Yang, Z. Xia, L. Ma, B. Chen, Y. Feng, and J. Zhang, "Experimental study on the influence of the injection structure on solid scramjet performance," *Acta Astronautica*, vol. 188, pp. 229–238, 2021.
- [40] S. K. Kireeti, G. R. K. Sastry, S. K. Gugulothu, B. Deepanraj, L. S. Sundar, and M. Arthi, "Comparison of combustion characteristics of four strut injectors with that of three strut injectors by numerically investigating doubly-dual cavity-based scramjet combustor," *Sustainable Energy Technologies and Assessments*, vol. 53, article 102759, 2022.
- [41] V. Sharma, V. Eswaran, and D. Chakraborty, "Influence of isolator section on the shock augmented mixing in scramjet engine," *Aerospace Science and Technology*, vol. 130, article 107900, 2022.

- [42] W. Li, X. Chen, O. Musa, L. Gong, and L. Zhu, "Investigation of the effect of geometry of combustor on combustion characteristics of solid-fuel ramjet with swirl flow," *Applied Thermal Engineering*, vol. 145, pp. 229–244, 2018.
- [43] C. Li, Y. Li, X. Chen, L. Zhu, and Y. Hou, "Assessment on the supersonic combustor performance induced by the asymmetric struts with hydrogen fuel," *International Journal of Hydrogen Energy*, vol. 45, no. 53, pp. 29560–29578, 2020.